Earth and Planetary Science Letters 518 (2019) 76–85

Contents lists available at ScienceDirect

Earth and Planetary Science Letters

www.elsevier.com/locate/epsl

Atmospheric flow deflection in the late Cenozoic Sierra Nevada

Hari T. Mix [a,*], Jeremy K. Caves Rugenstein [b,d,1], Sean P. Reilly [a], Andrea J. Ritch [b], Matthew J. Winnick [c,e], Tyler Kukla [c], C. Page Chamberlain [c]

[a] Department of Environmental Studies and Sciences, Santa Clara University, Santa Clara, CA 95053, USA
[b] Department of Earth System Science, Stanford University, Stanford, CA 94305, USA
[c] Department of Geological Sciences, Stanford University, Stanford, CA 94305, USA
[d] Department of Earth Sciences, ETH Zürich, 8092 Zürich, Switzerland
[e] Department of Geosciences, University of Massachusetts Amherst, Amherst, MA 01002, USA

ARTICLE INFO

Article history:
Received 20 August 2018
Received in revised form 25 April 2019
Accepted 30 April 2019
Available online xxxx
Editor: A. Yin

Keywords:
paleoaltimetry
paleoclimate
Sierra Nevada
stable isotopes
Basin and Range

ABSTRACT

Given the intimate links between topography, tectonics, climate, and biodiversity, considerable effort has been devoted to developing robust climate and elevation histories of orogens. In particular, quantitative geochemical reconstructions using stable oxygen and hydrogen isotopes have been applied to many of the world's mountain belts. Recent advances in atmospheric modeling have suggested that such stable isotope records from leeward sites can be affected by the complicating role that sufficiently elevated topography such as the southern (High) Sierra plays in diverting atmospheric circulation. While such "terrain blocking" effects are a hallmark feature of modern atmospheric circulation in the Sierra, their evolution remains poorly constrained. In order to examine the history of these terrain blocking effects, we developed stable isotope records from three late Cenozoic sedimentary basins in the Eastern Sierra and Basin and Range: 1) Authigenic clay minerals in the Mio-Pliocene Verdi Basin (VB) near present-day Reno, Nevada, 2) Fluvial and lacustrine carbonates from the Plio-Pleistocene Coso Basin (CB) in the southern Owens Valley, and 3) Miocene to Holocene pedogenic, fluvial and lacustrine carbonates of Fish Lake Valley (FLV). Whereas both the VB and CB are proximal to the Sierra crest, FLV is a distal leeward site east of the White and Inyo Mountains in the Basin and Range. The CB oxygen isotope record exhibits an increase of 1-2‰ over the last 6 Myr while VB and FLV show no significant change. These results suggest that terrain blocking around the southern Sierra initiated prior to the late Cenozoic, though it may have been modestly enhanced during the last 6 Ma.

1. Introduction

Topography is the physical expression of interactions between tectonic, Earth surface and atmospheric processes. Given the intimate links between topography and tectonics (Clark, 2007), climate (Seager et al., 2002), and biodiversity (Badgley et al., 2014), there has been widespread interest in developing accurate long-term topographic histories of orogens. In particular, quantitative reconstructions such as those using stable oxygen and hydrogen isotopes of geochemical proxies have been applied to many of the world's major mountain belts. Yet after decades of development, reconstructing the climate and elevation histories of orogens remains plagued with large uncertainties (Mulch, 2016). As stable isotope paleoclimatology and paleoaltimetry grow in use, so too do the discoveries of both the limitations and richness of terrestrial stable isotope records.

Stable isotope paleoaltimetry was initially applied within and on the leeward sides of orogens using modern empirical (Poage and Chamberlain, 2001) or one-dimensional thermodynamic models (e.g. Rowley et al., 2001) of stable isotope lapse rates. Traditionally, these studies have interpreted low oxygen or hydrogen isotope compositions ($\delta^{18}O$ and δD respectively) of minerals in the context of open-system Rayleigh distillation, as ^{18}O and D preferentially and progressively condense in precipitation (Dansgaard, 1964). Thus, negative temporal shifts in $\delta^{18}O$ and δD values are typically interpreted as signs of uplift. Complexities arise, however, in regions receiving moisture from multiple sources (Friedman et al., 2002), or where spatial or temporal differences in relief and/or humidity drive changes in post-condensation evaporation of precipitation (e.g., Blisniuk and Stern, 2005). Recent paleoaltimetry studies highlight the role of interactions between topographic de-

* Corresponding author.
E-mail address: hmix@scu.edu (H.T. Mix).
[1] Now at: Max Planck Institute for Meteorology, Bundesstr. 53, 20146 Hamburg, Germany.

https://doi.org/10.1016/j.epsl.2019.04.050
0012-821X/

velopment and the hydrologic cycle in dampening or obscuring altogether the paleoelevation signals predicted by one-dimensional thermodynamic models. Such heterogeneity in isotope-elevation relationships can be driven by changes in global temperature and pCO_2 (e.g., Molnar, 2010; Poulsen and Jeffery, 2011), deep convection (e.g., Rohrmann et al., 2014), and water vapor recycling (e.g., Mix et al., 2013; Chamberlain et al., 2014; Winnick et al., 2014).

Perhaps the most problematic of these interactions is the relationship between surface uplift and the deflection of atmospheric flow around sufficiently high and wide mountain ranges (e.g., Galewsky, 2009a, 2009b). Such "terrain blocking" effects can lead to reduced depletion of proxy $\delta^{18}O$ and δD values as a mountain range uplifts (or even increases in $\delta^{18}O$ and δD instead of the decreases as predicted by traditional paleoaltimetry) due to the contribution of relatively undistilled moisture that experiences reduced rainout as a result of not traversing the highest topography. Such trajectories are commonly observed in modern storm events, such as in atmospheric rivers, that divert around the Sierra Nevada in order to penetrate the western North American interior (Rutz et al., 2015). While terrain blocking is a prominent feature of modern atmospheric circulation of the central and southern Sierra at elevations in excess of 2.5 km (Lechler and Galewsky, 2013), atmospheric modeling suggests flow deflection similar to the present could have occurred as low as 2 km in a warmer and more stable mid-Miocene atmosphere (Wheeler et al., 2016). These complexities lead to potentially non-unique interpretations of leeward proxy stable isotope data: Shifts in $\delta^{18}O$ may be attributable to changing topography and consequent changes in orographic forcing of precipitation; or, alternatively, to background climatic changes that modify the same orographic forcing of precipitation but without any changes in the underlying topography.

Here, we use leeward stable isotope records to examine the history of atmospheric flow deflection in the late Cenozoic Sierra Nevada. The Sierra Nevada provides an ideal case for examining the complexities of stable isotope reconstructions. The proximity of the Sierra to its Pacific moisture source and the orientation of the range crest orthogonal to prevailing westerly flow throughout the Cenozoic make it an ideal orographic barrier for simple paleoaltimetry reconstructions. Today, the Sierra forms a large, westward tilted block, with the highest elevations consistently located along the eastern crest. The northern Sierra is characterized by modest elevations, with the highest peaks $\sim$3 km above sea level. The southern Sierra, also known as the High Sierra, contains the range's highest peaks, with many peaks in excess of 4 km and the highest peak standing 4.5 km above sea level.

Differences in the proposed evolution of the northern and southern Sierra lend themselves to examination of the interactions between topography and atmospheric circulation. The northern Sierra is widely recognized as a long-standing topographic feature (e.g., Gabet, 2014). Pioneering stable isotope work in the Sierra Nevada focused on the evidence for an isotopic rain shadow significantly to the lee of the Sierra in the Basin and Range (Taylor, 1974; Poage and Chamberlain, 2002). As spatial coverage of late Cenozoic stable isotope records improved, stable isotope transects across the Sierra Nevada and Basin and Range suggested that an elevation gradient across the Sierra similar to the present has existed since the Miocene (Mulch et al., 2008) or even the Cretaceous (e.g. Crowley et al., 2008). Unlike leeward paleoaltimetry, which could be susceptible to complications of terrain blocking, windward paleoaltimetry reconstructions using fluvial sediments have demonstrated that similar-to-modern elevation gradients existed on the windward side of the northern Sierra Nevada as early as the Eocene (Mulch et al., 2006; Cassel et al., 2009; Hren et al., 2010; Mix et al., 2015).

The southern Sierra, by contrast, has a more complex and debated late Cenozoic history. Unfortunately, windward paleoaltimetry is not possible in the southern Sierra. Even if the Cenozoic sediments required for stable isotope reconstructions once existed in the southern Sierra, they have since been eroded by the major river valleys (i.e. Tuolumne, Merced, Kings, Kern), which now incise into Mesozoic basement. The topographic history of the southern Sierra, however, has been closely examined. Some geomorphological evidence such as analysis of fluvial paleoslopes, knickpoints and tilted lavas are not consistent with late Cenozoic surface uplift (Gabet, 2014). Geological and geophysical evidence, however, are consistent with 1-2 km of late Cenozoic rock uplift in the southern Sierra Nevada (e.g., Stock et al., 2004; Zandt et al., 2004; Ducea and Saleeby, 1996). Some of these studies, however, invoke the delamination of an eclogitic root beneath the southern Sierra, whereas recent tomography work suggests this high-density anomaly may be a remnant of the Farallon Plate (Wang et al., 2013). Examination of displacement on the eastern Sierran escarpment suggests that the Sierra Nevada crest may have uplifted by several hundred meters to 1 km (Martel et al., 2014). Thus, though we acknowledge that the topographic history of the southern Sierra is debated, here we assume that the entire Sierra Nevada formed an orographic barrier at least 2 km in height, with the southern Sierra possibly higher or undergoing a modest amount of late Cenozoic uplift along the southern Sierran crest.

Given these independent constraints on the topographic evolution of the Sierra, what leeside stable isotope signatures would be expected from late Cenozoic topographic development and atmospheric flow deflection? As there is abundant evidence for terrain blocking in the modern Sierra, we posit that late Cenozoic leeside stable isotope records should be predominantly impacted by changes in the intensity of terrain blocking. In turn, if terrain blocking has increased (decreased) over the course of the late Cenozoic, we expect leeside stable isotope records to increase (decrease). Leeward of the northern Sierra Nevada, $\delta^{18}O$ or δD values would be relatively unchanged as trajectories would simply traverse the northern Sierran crest as they do in the present. Leeward of the southern Sierra Nevada, home to the highest elevations in the range, terrain blocking effects would produce more complex "wrap-around" trajectories south of the range. Thus, the onset of atmospheric flow deflection would likely drive an increase in $\delta^{18}O$ or δD values, as air mass trajectories transition from traversing moderately high elevations at the Sierran crest to lower elevations around the south of the range. As we treat the late Cenozoic uplift history of the Sierra Nevada as a constraint, the onset of atmospheric flow deflection may instead be more closely related to global climate, which became progressively cooler since the middle Miocene. Lechler and Galewsky (2013) observed atmospheric flow deflection around elevations $>$2.5 km in the present. Wheeler et al. (2016) modeled terrain blocking in the middle Miocene and showed that terrain blocking initiated at lower elevations (2 km) in the warmer, more stable atmosphere. Thus, if the warmer middle Miocene atmosphere does have an effect on terrain blocking, no stable isotope signal should be expected over the course of the late Cenozoic. If climate does not play a large role in terrain blocking, or if the southern Sierra underwent significant surface uplift in the late Cenozoic, an increase in $\delta^{18}O$ or δD values would be expected.

In order to test the history of terrain blocking in the Sierra Nevada, we developed three new stable isotope archives from the Eastern Sierra Nevada and Basin and Range: 1) Authigenic clay minerals from tephras in the Mio-Pliocene Verdi and Boca Basins (VB), 2) Fluvial and lacustrine carbonates from the Plio-Pleistocene Coso Basin (CB), and 3) Miocene to Holocene pedogenic, fluvial and lacustrine carbonates of Fish Lake Valley (FLV) (Fig. 1). A complete description of the geologic settings of these late Cenozoic basins, the archives they contain, and underlying references can be found in the **Supplementary Material**. Each of these sites has distinct

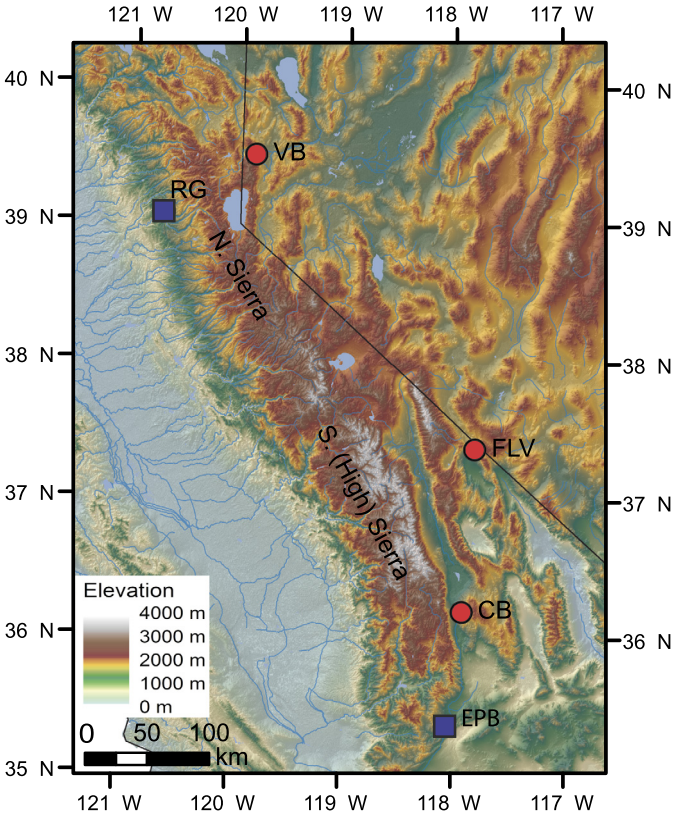

Fig. 1. Index map showing the locations of new Neogene stable isotope records (red circles) from the Verdi Basin (VB), Coso Basin (CB) and Fish Lake Valley (FLV). Additionally, the locations of published (blue squares) stable isotope records from the El Paso Basin (EPB) (Poage and Chamberlain, 2002) and Paleogene river gravels (RG) (Mulch et al., 2006; Cassel et al., 2009; Hren et al., 2010; Mix et al., 2015) are shown.

sources of surface and meteoric water, and therefore each has a distinct and independent response to late Cenozoic atmospheric circulation. Both VB (Reno) and CB (southern Owens Valley) are proximal to (just east of) the Sierra. However, while surface water was supplied to VB from the Sierran crest via the ancestral Truckee River throughout the Neogene (Trexler et al., 2012), the CB headwaters were in the Coso Mountains just east of the Sierra and therefore do not directly reflect the elevation of the southern Sierra Nevada crest. In contrast to both proximal sites, FLV lies to the east of the White-Inyo Mountains and therefore reflects distal leeward atmospheric moisture reaching the Basin and Range.

2. Stable isotope geochemistry

2.1. Stable isotope and X-ray diffraction methods

Carbonates were prepared and analyzed in the Stable Isotope Biogeochemistry Laboratory at Stanford University. Samples were prepared by using a handheld Dremel to produce a powder from the bulk sample. Weighed aliquots of the sample powders were loaded into sealed Exetainer vials and flush filled with helium gas. Samples were then reacted with phosphoric acid at 72 °C using a Thermo Finnigan GasBench and introduced into a Thermo Finnigan Delta^{Plus} XL mass spectrometer in a continuous flow configuration. Repeated analysis of NBS-19 and internal laboratory carbonate standards demonstrated the precision of this method to be $<0.2‰$ for both $\delta^{18}O$ and $\delta^{13}C$.

Tephra samples were prepared in the Stable Isotope Laboratory at Santa Clara University. Bulk samples were broken with a hammer and blended if necessary. Approximately 200 g of unconsolidated material was suspended in deionized water and passed through a No. 100 sieve. The <0.5 µm size fraction was isolated by centrifugation using a Beckman Allegra X-14 benchtop centrifuge. We used X-ray diffractometry on all tephras to identify smectite and eliminate samples characterized by non-smectite minerals (e.g. Moore and Reynolds, 1997). Samples were gently powdered with a mortar and pestle, suspended in isopropanol, and left to air-dry on a zero-background quartz sample holder. Analyses were performed at the Stanford University Environmental Measurements Facility using a Rigaku MiniFlex 600 Benchtop X-ray Diffraction System equipped with a Cu anode set at the maximum power of 600 W. Each sample was analyzed under two measurement conditions: 1) Coarse resolution with 2-theta ranging 2-90 degrees, and 2) High resolution with 2-theta ranging 2-30 degrees. Coarse and fine resolution measurements were performed for both dry and glycolated sample powders. To glycolate, samples were placed in a sealed desiccator with one centimeter of ethylene glycol at the base and left overnight in an oven set to 65 °C (Poppe et al., 2001). We used the Rigaku PDXL software to aid in mineral identification in each sample.

Hydrogen isotope analysis of authigenic clays was performed at the Stable Isotope Biogeochemistry Laboratory at Stanford University following procedures similar to Mix and Chamberlain (2014). Samples were enclosed in silver foil, then placed in a Fisher Scientific Isotemp vacuum oven at 80 °C and −100 kPa pressure for at least 3 days before isotopic analysis. Each sample was pyrolyzed at 1450 °C using a Thermo Scientific TC/EA high temperature conversion elemental analyzer. Hydrogen isotope composition was determined with a Thermo Finnigan Delta^{Plus}XL mass spectrometer in continuous flow mode. Analyses were controlled by measurements of NBS-22 oil and polyethylene foil (PEF1) international reference materials. Instrumental error for this method is less than 2‰. All isotope ratios are reported relative to Vienna Standard Mean Ocean Water (V-SMOW).

2.2. Stable isotope results

Clay mineral δD values in the Verdi and Boca Basins ($n = 14$) show little change from late Miocene to Pleistocene with a range of δD values of −100 to −80‰ (Fig. 2A). A linear regression through the data indicates a slope of $\sim -1‰/Myr \pm 0.4‰$ (1σ) in δD that is not statistically distinguishable from a slope of zero ($p = 0.019$). Given that variation in hydrogen isotope composition of meteoric water is ∼8x that of oxygen, this is a slope of $<0.2‰$ in $\delta^{18}O$ space. Thus, we interpret the clay mineral record to reflect relative stability throughout the late Cenozoic in the Verdi and Boca Basins.

Miocene to Pleistocene carbonate $\delta^{18}O$ values from Fish Lake Valley, CA-NV range from 15.3 to 18.5‰, excluding an evaporitic interval (the "Playa" subsection) from ∼2.8 to 2.3 Ma (Fig. 2B). Late Miocene samples of the Horse Thief Canyon subsection have a mean $\delta^{18}O$ value of 16.64 ± 0.9, 1σ ($n = 36$). In nearby Willow Wash, $\delta^{18}O$ values increase upsection from the Pliocene "Black Hole" subsection (15.79 ± 0.5, 1σ, $n = 18$) to the Pliocene-Pleistocene "Badlands" subsection (17.34 ± 0.4, 1σ, $n = 9$). We also collected and analyzed 4 samples from the Pliocene "Playa" subsection, which ranged from 19.9 to 27.0‰. Given that: 1) "Playa" $\delta^{18}O$ values are all greater than other Fish Lake Valley carbonates; 2) we observed abundant evaporite minerals such as gypsum in this depositional interval; and, 3) this section has been previously interpreted as an evaporitic lake (e.g., Reheis et al., 1991), we excluded these samples from our interpretations of meteoric water oxygen isotope composition. Though the record exhibits multiple trends, including a decrease in $\delta^{18}O$ values during the early Pliocene between the Horse Thief Canyon and Black Hole subsections, the overall linear regression trend is a minor (<0.2 ±

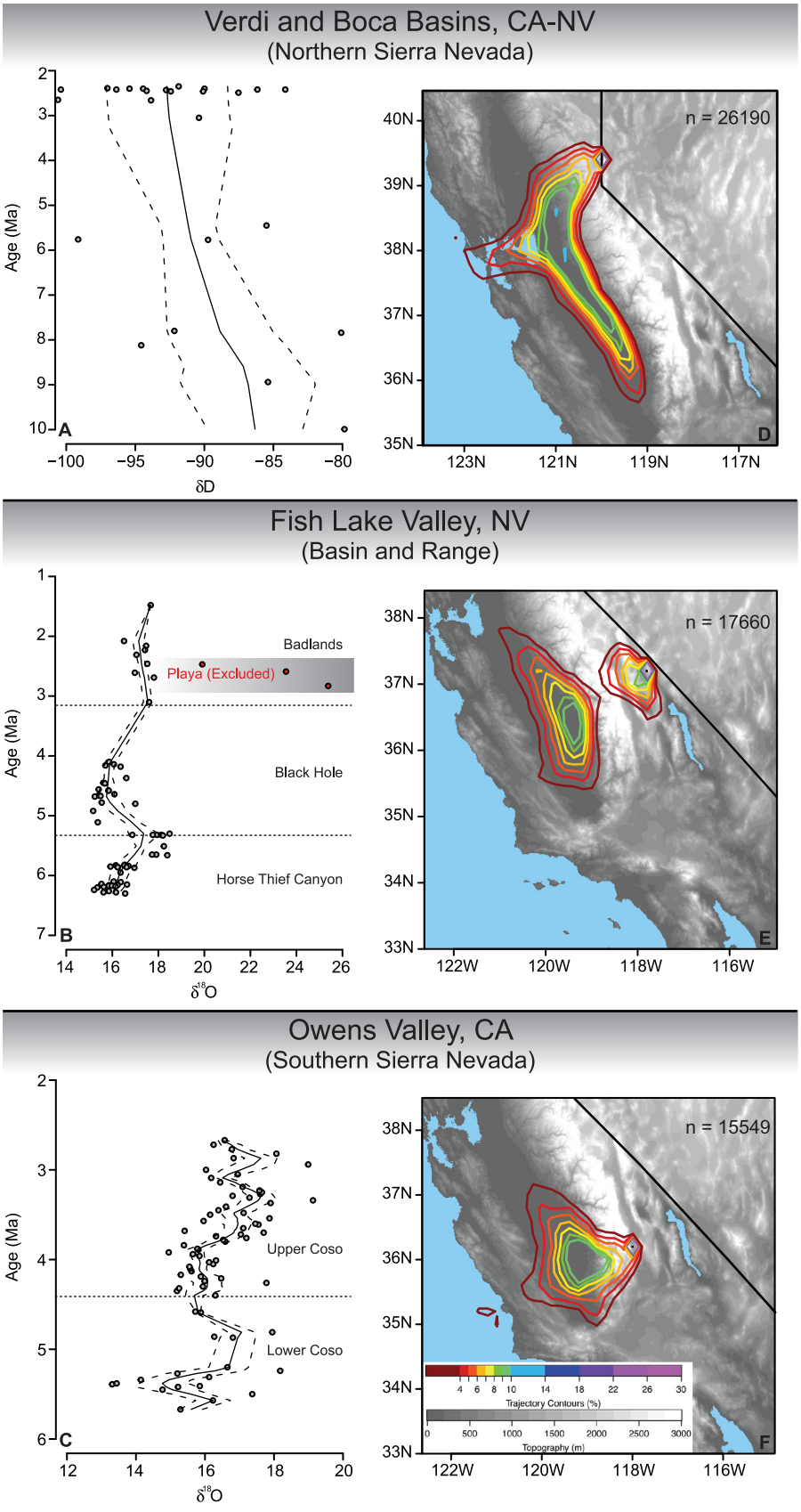

Fig. 2. Neogene stable isotope data (A-C) and modern annual air parcel back-trajectory analysis (D-F) from the Verdi and Boca Basins, CA-NV, Fish Lake Valley, NV, and Owens Valley, CA. Stable isotope data are smoothed with an Epanechnikov kernel with a 1 Ma bandwidth (solid line; $+/-1\sigma$ are dashed lines). Air parcel back-trajectories are contoured by 0.2° x 0.2°. n indicates total number of 4-day back-trajectories contoured.

0.09‰/Myr, 1σ) increase in δ^{18}O through the composite section that is not significantly different from no change in the record (p = 0.034). As with the Verdi and Boca Basins, to first order we interpret the Fish Lake Valley record to reflect no long-term change in δ^{18}O.

Carbonate δ^{18}O values in the Owens Valley, CA increase between 6 and 2 Ma by approximately 2‰. The first order change in δ^{18}O, by linear regression, is 0.65 ± 0.14‰/Myr (1σ) and is significantly different from zero (p = 1.42x10^{-5}). The late Miocene portion of the Lower Coso subsection have a mean δ^{18}O value of 15.2 ± 1.3, 1σ (n = 10). The late Pliocene portion of the Upper Coso section trends to more ^{18}O-enriched values (17.1 ± 0.9, 1σ, n = 25) (Fig. 2C). The Coso Basin composite section records a ~1‰ δ^{18}O decrease during the early Pliocene (5 to 4.2 Ma) similar to the shift observed in FLV.

We performed a linear regression analysis of the oxygen or hydrogen isotope composition through time and determined statistical significance by assigning a p-value to the regression slope being different than zero. Our chosen significance level was 0.01, which is lower than a typical significance level of p < 0.05 to account for limitations in sample resolution. Part of the reason for a statistically-significant long-term trend in Owens Valley is due to the high sampling density throughout the Owens Valley section, which permits resolution of a long-term trend in δ^{18}O. The lack of a significant trend in the Fish Lake Valley record, despite a seemingly similar long-term increase in δ^{18}O (Fig. 2), may result from poor sampling density in the upper part of the section. Similarly, in the Verdi and Boca Basin record, we lack sufficient sampling density within the lower part of the section to resolve any long-term trend in δD. Consequently, more work, at higher-resolution through both sections, is needed to determine if long-term changes in δD or in δ^{18}O are evident. Nevertheless, for the purposes of this manuscript, we interpret the Verdi/Boca Basin and Fish Lake Valley records as displaying no long-term change in δD and δ^{18}O, respectively.

3. Back-trajectory analysis

In order to determine the dominant trajectories of atmospheric moisture in the modern Sierra Nevada region, we used the Hybrid Single-Particle Lagrangian Trajectory Model (HYSPLIT) (Draxler and Hess, 1998). HYSPLIT back-trajectory analysis has been applied to determine modern moisture transport pathways and to interpret stable isotope paleoclimate archives (e.g., Sjostrom and Welker, 2009; Bershaw et al., 2012; Lechler and Galewsky, 2013; Caves et al., 2014; Caves et al., 2017). We used the high resolution (~32 x 32 km) North American Regional Reanalysis (NARR) dataset to analyze air mass trajectories that end at each of our three late Cenozoic sedimentary archives. Here, we report only those trajectories that produce precipitation within 6 h of the endpoint. To account for precipitation that might be produced at different levels in the atmosphere, we initialize back-trajectories at 3 different heights (1000 m, 1500 m, and 2000 m), which spans the height at which most moisture is transported (e.g., Bershaw et al., 2012). At each level, we analyzed a total of 50,120 4-day back-trajectories initiated at 6-h intervals between 1980 and 2014 for a total of 150,360 trajectories at each site. This approach is similar to that of Lechler and Galewsky (2013), though it differs in several ways. We analyzed precipitating backtrajectories specifically at our stable isotope field sites, binned them by season (see **Supplementary Material**), and initialized trajectories at different heights. Ultimately, these methods yielded similar results to Lechler and Galewsky (2013), demonstrating that HYSPLIT initializations and seasonality do not drive the results presented here.

Our results illustrate differences in the primary moisture transport pathways at sites in the Eastern Sierra Nevada and Basin and Range. In the Verdi Basin of the northeastern Sierra, moisture is transported northward along the rangefront in the Sierra Barrier Jet before joining westerly trajectories and traversing eastward over the range crest (Fig. 2D). In contrast, precipitating trajectories in Owens Valleys (Fig. 2F) shows moisture pathways that are redirected around the most elevated topography (greater than ~2-2.5 km) by flowing to the south of the High Sierra. Finally, Fish Lake Valley trajectories (Fig. 2E) exhibit an unusual pattern of clustering on the eastern and western Sierra. As the contours reflect the time spent over a location, the clustered pattern suggests that trajectories slow down or stagnate over the Central Valley before traversing the crest at a quicker rate. Trajectories binned seasonally largely resemble the combined annual contour plots with the most significant deviations from the annual plots occurring during the summer months (JJA), which are strongly influenced by southerly moisture from the Gulf of California (**Supp. Fig. 1**). At the southern Owens Valley and Fish Lake Valley sites, there is more influence of southerly-sourced moisture as opposed to westerly moisture, which dominates during the non-summer months. This likely points to the increased influence of the North American Monsoon, with the Gulf of California supplementing the Pacific moisture source. The number of precipitating trajectories in the summer months is significantly less (~4-7x) than those in the winter. This matches the winter/spring-wet modern climatology, with 50-75% of precipitation occurring between December and May at these three sites (Intellicast, 2018).

4. Discussion

Late Cenozoic sedimentary records reveal multiple trends in the stable isotope composition of waters adjacent to the northern and southern Sierra Nevada (see Table 1). The hydrogen isotope composition of authigenic clays in the Verdi and Boca Basins (VB) in the northern Sierra remain constant between 10 and 2 Ma. Values of δ^{18}O in the Owens Valley (CB) east of the southern Sierra increase by ~2‰ over the last 6 Ma, an increase that we find to be robust, while those in Fish Lake Valley (FLV) exhibit a not statistically robust increase of ~1-2‰ during the same interval. Any long-term trend in VB or FLV is overshadowed by internal variability that would need to be resolved with greater sampling density. Below, we evaluate these late Cenozoic stable isotope records in the context of atmospheric flow deflection.

How would atmospheric flow deflection be recorded leeward of the late Cenozoic Sierra Nevada? The Sierra Nevada likely formed an orographic barrier of moderate (~3 km average maximum elevations) height with west to east laminar flow over both the northern and southern parts of the range prior to the late Cenozoic (e.g., Gabet, 2014) (Fig. 3A). Subsequent uplift, if any, was restricted to the southern Sierra, which at some point became sufficiently elevated to deflect atmospheric flow (Fig. 3B). In the northern Sierra (Verdi and Boca Basins), we would expect no stable isotope response, as modern trajectories consistently traverse the range crest from west to east (i.e. minimal blocking effects). Therefore, we interpret the consistent δD of clay minerals in the Verdi region throughout the late Cenozoic (Fig. 2A) to reflect unchanging hypsometric mean elevation of the Sierra crest, which has been elevated in this portion of the range since early Cenozoic (e.g., Mulch et al., 2006; Cassel et al., 2009; Hren et al., 2010; Mix et al., 2015).

In the southern Sierra (Coso Basin in Owens Valley), the development of terrain blocking would lead to an increase in δ^{18}O as air masses no longer traverse the Sierran crest, but rather wrap around the highest topography. Here, we observe a statistically significant increase in δ^{18}O of ~2‰ in carbonate δ^{18}O values over the last 6 Ma within the section (the probability that there is no change in δ^{18}O through the record is < 0.01% based on lin-

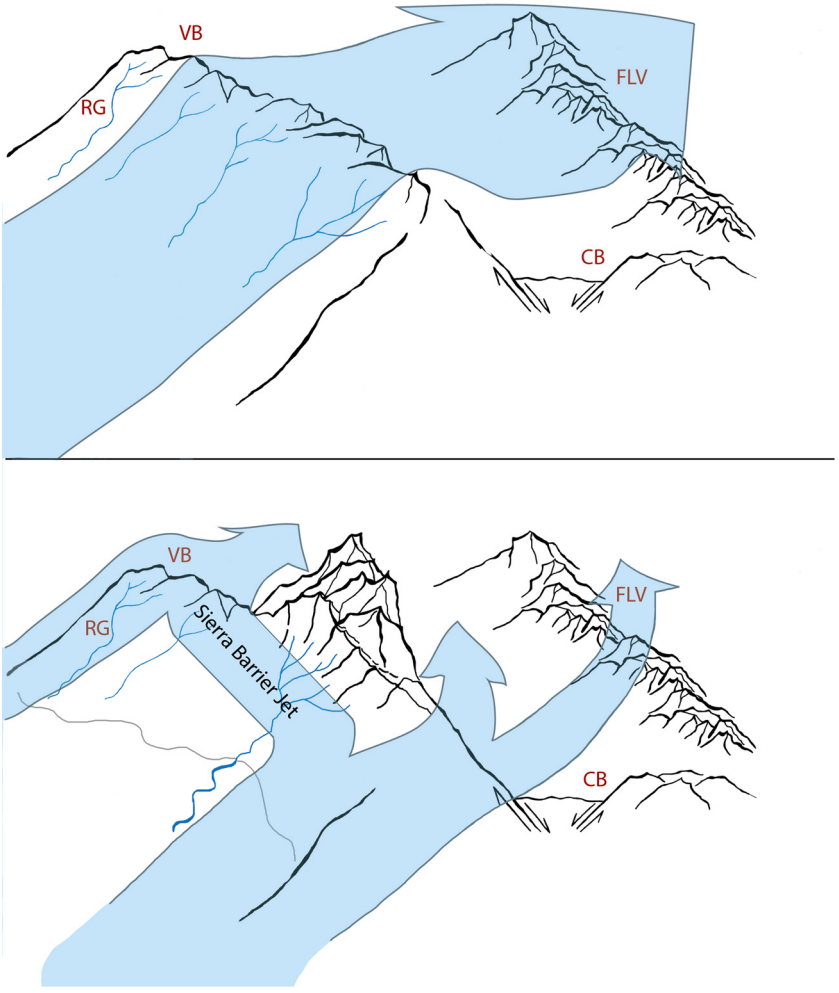

Fig. 3. Schematic diagram of atmospheric flow before and after uplift of the southern Sierra. (A) Hypothetical pre-existing northern and southern Sierra of moderate (2-2.5 km) height with flow passing over the range at all sites. (B) Following uplift to modern heights, development of atmospheric flow deflection around southern Sierra and the Sierra Barrier Jet are shown. (RG) Paleogene River Gravels, (VB) Verdi and Boca Basins, (FLV) Fish Lake Valley, and (CB) Coso Basin.

ear regression analysis). This $\delta^{18}O$ increase could be explained by an increase in the fraction of moisture that traveled around, rather than over, the southern Sierra through time. Using a modern global stable isotope lapse rate of $-2.8‰$/km (Poage and Chamberlain, 2001), a change in trajectory from traversing a 2-2.5 km Sierran crest to 1-1.5 km high modern topography adjacent to the range would correspond to an increase of $\sim$1.4 – 4.2‰. Further East, Fish Lake Valley lies in a zone where moisture reconverges leeward of the Sierra and therefore represents a mixing of these two end-members, as this region receives input of moisture traversing the northernmost Sierra and Modoc Plateau as well as moisture deflected to the south of the Sierra. Here again, we observe no statistically significant increase in $\delta^{18}O$ values (Fig. 2B). Overall, changes in terrain blocking, if any, were small during the late Cenozoic.

Given that we only observe one statistically significant modest increase in these late Cenozoic, leeward, stable isotope records our findings suggest that terrain blocking has been a long-standing feature of atmospheric circulation in the southern Sierra Nevada. The change of only $\sim$2‰ in the Coso Basin (CB) is more consistent with strengthening, rather than the onset, of blocking. These results are consistent with the modeling work of Wheeler et al. (2016), which demonstrated that terrain blocking could occur around elevations as low as 2 km in a warmer middle Miocene atmosphere. This suggests that the southern Sierra reached elevations of 2 km at least as early as the middle Miocene, though the small $\delta^{18}O$ increases in CB and FLV could be consistent with modest surface uplift in the late Cenozoic.

Existing Basin and Range records provide an interesting comparison to those of this study. Nearly all published late Cenozoic stable isotope records in the Basin and Range increase on the order of 2-6‰ in $\delta^{18}O$ – significantly larger than those of this study (Mix et al., 2013). Relatively close to the Sierra, Poage and Chamberlain (2002) observed a 5-6‰ oxygen isotope increase in the El Paso Basin east of the southernmost Sierra and a 2-3‰ increase in a composite section to the north of El Paso Basin in the western Basin and Range. These increases, along with those observed by Horton and Chamberlain (2006) in the central Basin and Range, have been attributed to topographic downdrop of the Basin and Range and/or Sierra. In contrast to these studies, the records presented here are more proximal to the Sierra and therefore, more reliably reflect changes in Sierran paleoelevation rather than topographic or climatic conditions more distal to the range. As the records of this study are relatively unchanged, we argue that surface elevations (and concomitant atmospheric circulation) have remained consistent throughout the late Cenozoic.

While a number of additional factors related to climate and atmospheric circulation are known to influence stable isotope records, none are sufficient to accommodate the signatures we observe in all three late Cenozoic sedimentary archives. We observe an increase of 2‰ in $\delta^{18}O$ in CB and no significant change

Table 1
Stable isotope composition of clay and carbonate minerals, eastern Sierra Nevada, California-Nevada.

Sample	Location	Age (Ma)	δD (‰ VSMOW)	δD Error (1σ)	$\delta^{18}O$ (‰ VSMOW)	$\delta^{18}O$ Error (1σ)	$\delta^{13}C$ (‰ VPDB)	$\delta^{13}C$ Error (1σ)	Material
Coso Basin, CA									
LC4	(36.2022 °N, 117.9106 °W)	5.67	–	–	15.29	0.02	−0.29	0.07	Marl
LC8	(36.2022 °N, 117.9106 °W)	5.57	–	–	16.23	0.09	1.08	0.08	Limestone
LC9	(36.2022 °N, 117.9106 °W)	5.50	–	–	17.37	0.02	−0.48	0.06	Limestone
LC10	(36.2022 °N, 117.9106 °W)	5.45	–	–	14.77	0.06	−0.54	0.07	Limestone
LC11	(36.2022 °N, 117.9106 °W)	5.42	–	–	15.22	0.07	−0.43	0.05	Limestone
LC13	(36.2022 °N, 117.9106 °W)	5.41	–	–	15.85	0.10	−0.30	0.07	Lacustrine carbonate
LC14	(36.2022 °N, 117.9106 °W)	5.39	–	–	13.31	0.05	0.15	0.06	Lacustrine carbonate
LC15	(36.2022 °N, 117.9106 °W)	5.38	–	–	13.44	0.09	0.22	0.10	Limestone
LC16	(36.2022 °N, 117.9106 °W)	5.34	–	–	14.14	0.12	−0.36	0.06	Marl
LC17	(36.2022 °N, 117.9106 °W)	5.31	–	–	16.12	0.12	−0.51	0.13	Calcite cemented sand
LC18	(36.2022 °N, 117.9106 °W)	5.27	–	–	15.20	0.06	0.37	0.06	Limestone
LC19	(36.2022 °N, 117.9106 °W)	5.24	–	–	18.18	0.03	1.76	0.03	Limestone
LC20	(36.2022 °N, 117.9106 °W)	5.20	–	–	16.65	0.09	0.36	0.12	Sandy limestone
LC21	(36.2022 °N, 117.9106 °W)	4.87	–	–	16.81	0.06	0.31	0.03	Limestone
LC22	(36.2022 °N, 117.9106 °W)	4.86	–	–	16.27	0.04	−0.14	0.04	Massive Limestone
LC23	(36.2022 °N, 117.9106 °W)	4.81	–	–	17.95	0.04	1.19	0.07	Massive Limestone
LC24	(36.2022 °N, 117.9106 °W)	4.59	–	–	15.88	0.07	−0.23	0.09	Lacustrine carbonate
LC25	(36.2022 °N, 117.9106 °W)	4.58	–	–	15.72	0.05	0.81	0.05	Lacustrine carbonate
LC26	(36.2022 °N, 117.9106 °W)	4.40	–	–	16.30	0.07	1.27	0.06	Lacustrine carbonate
UC1	(36.2008 °N, 117.9152 °W)	4.35	–	–	15.19	0.09	−0.23	0.10	Lacustrine carbonate
UC2	(36.2008 °N, 117.9152 °W)	4.32	–	–	15.25	0.06	−0.82	0.04	Lacustrine carbonate
UC3	(36.2008 °N, 117.9152 °W)	4.30	–	–	15.94	0.09	0.10	0.09	Lacustrine carbonate
UC5	(36.2008 °N, 117.9152 °W)	4.26	–	–	17.78	0.06	−0.59	0.12	Lacustrine carbonate
UC6	(36.2008 °N, 117.9152 °W)	4.24	–	–	15.99	0.08	−0.66	0.10	Lacustrine carbonate
UC7	(36.2008 °N, 117.9152 °W)	4.21	–	–	16.47	0.07	0.07	0.08	Lacustrine carbonate
UC8	(36.2008 °N, 117.9152 °W)	4.19	–	–	15.88	0.07	−0.26	0.09	Lacustrine carbonate
UC9	(36.2008 °N, 117.9152 °W)	4.17	–	–	15.30	0.07	−1.31	0.08	Lacustrine carbonate
UC10	(36.2008 °N, 117.9152 °W)	4.13	–	–	15.61	0.07	−0.46	0.05	Red, blocky carbonate
UC11	(36.2008 °N, 117.9152 °W)	4.10	–	–	15.57	0.06	−0.34	0.06	Lacustrine carbonate
UC12	(36.2008 °N, 117.9152 °W)	4.08	–	–	15.55	0.07	−0.33	0.13	Lacustrine carbonate
UC13	(36.2008 °N, 117.9152 °W)	4.05	–	–	16.24	0.08	−0.44	0.06	Lacustrine carbonate
UC14	(36.2008 °N, 117.9152 °W)	4.03	–	–	16.12	0.07	−0.01	0.14	Lacustrine carbonate
UC15	(36.2008 °N, 117.9152 °W)	4.01	–	–	16.32	0.09	−0.51	0.09	Lacustrine carbonate
UC16	(36.2008 °N, 117.9152 °W)	3.96	–	–	15.84	0.04	−0.74	0.08	Lacustrine carbonate
UC17	(36.2008 °N, 117.9152 °W)	3.94	–	–	15.65	0.08	−0.53	0.06	Lacustrine carbonate
UC18	(36.2008 °N, 117.9152 °W)	3.92	–	–	14.95	0.07	−0.76	0.01	Lacustrine carbonate
UC19	(36.2008 °N, 117.9152 °W)	3.89	–	–	15.81	0.10	−0.79	0.04	Lacustrine carbonate
UC20	(36.2008 °N, 117.9152 °W)	3.88	–	–	15.78	0.05	−1.23	0.10	Lacustrine carbonate
UC21	(36.2008 °N, 117.9152 °W)	3.84	–	–	15.39	0.06	−1.18	0.08	Lacustrine carbonate
UC22	(36.2008 °N, 117.9152 °W)	3.80	–	–	16.59	0.07	−1.16	0.09	Lacustrine carbonate
UC23	(36.2008 °N, 117.9152 °W)	3.78	–	–	16.53	0.10	−0.89	0.08	Lacustrine carbonate
UC24	(36.2008 °N, 117.9152 °W)	3.76	–	–	17.20	0.04	−1.20	0.04	Lacustrine carbonate
UC25	(36.2008 °N, 117.9152 °W)	3.74	–	–	16.32	0.12	−0.50	0.10	Lacustrine carbonate
UC26	(36.2008 °N, 117.9152 °W)	3.72	–	–	17.04	0.12	−0.85	0.10	Lacustrine carbonate
UC27	(36.2008 °N, 117.9152 °W)	3.70	–	–	17.70	0.05	−1.28	0.07	Lacustrine carbonate
UC28	(36.2008 °N, 117.9152 °W)	3.68	–	–	15.41	0.04	−1.52	0.09	Lacustrine carbonate
UC29	(36.2008 °N, 117.9152 °W)	3.65	–	–	17.11	0.04	−1.97	0.07	Lacustrine carbonate
UC30	(36.2008 °N, 117.9152 °W)	3.61	–	–	17.55	0.08	−1.41	0.09	Lacustrine carbonate
UC31	(36.2008 °N, 117.9152 °W)	3.60	–	–	17.46	0.09	−1.23	0.05	Lacustrine carbonate
UC32	(36.2008 °N, 117.9152 °W)	3.57	–	–	15.96	0.06	−1.29	0.07	Lacustrine carbonate
UC33	(36.2008 °N, 117.9152 °W)	3.54	–	–	17.87	0.08	−1.15	0.06	Lacustrine carbonate
UC34	(36.2008 °N, 117.9152 °W)	3.50	–	–	16.15	0.12	−1.61	0.06	Lacustrine carbonate
UC35	(36.2008 °N, 117.9152 °W)	3.48	–	–	17.12	0.07	−1.19	0.10	Lacustrine carbonate
UC36	(36.2008 °N, 117.9152 °W)	3.45	–	–	16.39	0.07	−0.84	0.10	Lacustrine carbonate
UC38	(36.2008 °N, 117.9152 °W)	3.41	–	–	16.61	0.08	−1.55	0.08	Lacustrine carbonate
UC39	(36.2008 °N, 117.9152 °W)	3.37	–	–	17.90	0.13	−1.17	0.12	Lacustrine carbonate
UC40	(36.2008 °N, 117.9152 °W)	3.34	–	–	19.13	0.09	−1.24	0.03	Lacustrine carbonate
UC42	(36.2008 °N, 117.9152 °W)	3.31	–	–	17.29	0.13	−2.64	0.10	Lacustrine carbonate
UC44	(36.2008 °N, 117.9152 °W)	3.29	–	–	16.80	0.08	−1.55	0.05	Lacustrine carbonate
UC45	(36.2008 °N, 117.9152 °W)	3.27	–	–	17.60	0.06	−1.17	0.06	Lacustrine carbonate
UC46	(36.2008 °N, 117.9152 °W)	3.25	–	–	17.65	0.10	−0.95	0.05	Lacustrine carbonate
UC47	(36.2008 °N, 117.9152 °W)	3.23	–	–	17.58	0.09	−0.36	0.09	Lacustrine carbonate
UC48	(36.2008 °N, 117.9152 °W)	3.19	–	–	17.09	0.07	−1.21	0.10	Lacustrine carbonate
UC49	(36.2008 °N, 117.9152 °W)	3.14	–	–	16.44	0.07	−1.11	0.11	Lacustrine carbonate
UC50	(36.2008 °N, 117.9152 °W)	3.09	–	–	16.18	0.08	−1.80	0.11	Lacustrine carbonate
UC51	(36.2008 °N, 117.9152 °W)	3.05	–	–	16.95	0.10	−1.08	0.06	Lacustrine carbonate
UC52	(36.2008 °N, 117.9152 °W)	3.00	–	–	16.03	0.09	−1.13	0.07	Lacustrine carbonate
UC53	(36.2008 °N, 117.9152 °W)	2.94	–	–	18.99	0.05	−0.32	0.09	Lacustrine carbonate
UC54	(36.2008 °N, 117.9152 °W)	2.87	–	–	16.83	0.03	−1.43	0.09	Lacustrine carbonate
UC55	(36.2008 °N, 117.9152 °W)	2.82	–	–	18.07	0.07	−1.08	0.07	Lacustrine carbonate
UC56	(36.2008 °N, 117.9152 °W)	2.77	–	–	16.78	0.10	−0.95	0.07	Lacustrine carbonate
UC57	(36.2008 °N, 117.9152 °W)	2.72	–	–	16.25	0.09	0.07	0.08	Lacustrine carbonate
UC58	(36.2008 °N, 117.9152 °W)	2.67	–	–	16.57	0.06	−1.16	0.02	Lacustrine carbonate

Table 1 (*continued*)

Sample	Location	Age (Ma)	δD (‰ VSMOW)	δD Error (1σ)	δ^{18}O (‰ VSMOW)	δ^{18}O Error (1σ)	δ^{13}C (‰ VPDB)	δ^{13}C Error (1σ)	Material
Verdi and Boca Basins, CA-NV									
VB1	(39.5124 °N, 119.859 °W)	2.35	−91.86	0.25	–	–	–	–	Reworked tephra
VB10	(39.4951 °N, 119.8551 °W)	2.39	−97.02	1.25	–	–	–	–	Silty white tephra lens
VB11	(39.4951 °N, 119.8548 °W)	2.40	−94.43	1.60	–	–	–	–	White silty tephra
VB12	(39.4951 °N, 119.8547 °W)	2.40	−89.99	0.66	–	–	–	–	Blocky whitish gray tephra
VB13	(39.4951 °N, 119.8547 °W)	2.40	−95.42	1.23	–	–	–	–	White tephra
VB14	(39.4950 °N, 119.8546 °W)	2.42	−100.39	0.74	–	–	–	–	Platey white tephra
VB15	(39.4950 °N, 119.8546 °W)	2.42	−96.37	2.27	–	–	–	–	Flakey gray clay
VB3	(39.5124 °N, 119.8599 °W)	2.42	−86.16	1.48	–	–	–	–	Light colored tephra
VB4	(39.5124 °N, 119.8596 °W)	2.42	−84.14	0.14	–	–	–	–	Fine-grained tephra
VB5	(39.5123 °N, 119.8597 °W)	2.43	−92.77	1.87	–	–	–	–	Fine-grained tephra
VB16	(39.4950 °N, 119.8544 °W)	2.45	−94.18	0.77	–	–	–	–	White flakey tephra
VB17	(39.4950 °N, 119.8542 °W)	2.46	−92.43	2.19	–	–	–	–	Brownish reworked tephra sandstone
VB18	(39.4950 °N, 119.8542 °W)	2.46	−90.09	0.43	–	–	–	–	Tan reworked tephra sandstone
VB19	(39.4950 °N, 119.8542 °W)	2.49	−87.53	0.49	–	–	–	–	Light gray tephra sandstone
VB20	(39.4950 °N, 119.8542 °W)	2.65	−100.60	0.76	–	–	–	–	Clay-rich weathered sandstone
VB21	(39.4950 °N, 119.8542 °W)	2.66	−93.86	1.38	–	–	–	–	White chalky tephra
BR2	(39.4920 °N, 120.1076 °W)	3.05	−90.39	1.52	–	–	–	–	Chalk Hills Ash
VB24	(39.4946 °N, 119.8853 °W)	5.45	−85.50	1.19	–	–	–	–	Gray flakey clay-rich tephra
VB23	(39.4947 °N, 119.8807 °W)	5.76	−99.14	0.85	–	–	–	–	Loose white flakey tephra
VB22	(39.4946 °N, 119.8811 °W)	5.77	−89.73	1.87	–	–	–	–	Thin fluvial tephra
VB25	(39.4917 °N, 119.8971 °W)	7.80	−92.17	1.39	–	–	–	–	Blocky reworked tephra
VB26	(39.4919 °N, 119.8962 °W)	7.84	−80.09	0.81	–	–	–	–	Blocky gray clay
VB6	(39.5033 °N, 119.8923 °W)	8.12	−94.57	1.47	–	–	–	–	Dark brown clay
VB28	(39.5008 °N, 119.9008 °W)	8.94	−85.39	2.38	–	–	–	–	Tan blocky reworked tephra
VB8	(39.5044 °N, 119.9012 °W)	9.99	−79.85	1.48	–	–	–	–	Dense white tephra
Fish Lake Valley, NV									
Horse Thief Canyon									
FL1	(37.3433 °N, 117.8383 °W)	5.30	–	–	18.49	0.07	−3.72	0.06	Caliche
FL2	(37.3433 °N, 117.8383 °W)	5.32	–	–	17.94	0.03	−3.89	0.03	Caliche
FL4	(37.3433 °N, 117.8383 °W)	5.32	–	–	17.76	0.11	−2.28	0.12	Carbonate cement
FL5	(37.3433 °N, 117.8383 °W)	5.32	–	–	16.87	0.06	−2.32	0.05	Carbonate cement
FL6	(37.3433 °N, 117.8383 °W)	5.32	–	–	18.13	0.14	−4.15	0.10	Carbonate cement
FL7	(37.3433 °N, 117.8383 °W)	5.33	–	–	18.20	0.15	−2.14	0.11	Carbonate cement
FL12	(37.3433 °N, 117.8383 °W)	5.51	–	–	18.24	0.15	−3.96	0.09	Carbonate cement
FL16	(37.3433 °N, 117.8383 °W)	5.65	–	–	17.91	0.05	−3.30	0.05	Carbonate cement
FL17	(37.3433 °N, 117.8383 °W)	5.65	–	–	17.73	0.02	−4.00	0.05	Carbonate cement
FL18	(37.3433 °N, 117.8383 °W)	5.66	–	–	18.39	0.04	−3.36	0.06	Carbonate cement
FL19	(37.3433 °N, 117.8383 °W)	5.82	–	–	16.54	0.05	−6.27	0.07	Carbonate cemented tephra
FL20	(37.3433 °N, 117.8383 °W)	5.83	–	–	16.52	0.09	−5.09	0.09	Carbonate cement
FL21	(37.3433 °N, 117.8383 °W)	5.83	–	–	16.15	0.10	−5.38	0.08	Carbonate cement
FL22	(37.3433 °N, 117.8383 °W)	5.84	–	–	16.70	0.04	−4.98	0.09	Carbonate cement
FL24	(37.3433 °N, 117.8383 °W)	5.85	–	–	15.92	0.07	−6.65	0.11	Carbonate cemented tephra
FL25	(37.3433 °N, 117.8383 °W)	5.86	–	–	16.25	0.04	−5.65	0.05	Carbonate cement
FL26	(37.3433 °N, 117.8383 °W)	5.86	–	–	16.23	0.04	−5.64	0.04	Limestone
FL27	(37.3433 °N, 117.8383 °W)	5.86	–	–	16.62	0.09	−5.50	0.14	Carbonate cement
FL28	(37.3433 °N, 117.8383 °W)	5.87	–	–	16.96	0.06	−5.17	0.07	Carbonate cement
FL31	(37.3433 °N, 117.8383 °W)	5.95	–	–	16.36	0.09	−5.68	0.09	Carbonate cement
FL34	(37.3433 °N, 117.8383 °W)	6.10	–	–	16.06	0.05	−4.68	0.07	Carbonate cement
FL35	(37.3433 °N, 117.8383 °W)	6.11	–	–	16.37	0.09	−5.32	0.08	Carbonate cement
FL36b	(37.3433 °N, 117.8383 °W)	6.14	–	–	15.53	0.06	−4.99	0.13	Carbonate cement
FL37	(37.3433 °N, 117.8383 °W)	6.15	–	–	16.64	0.08	−4.30	0.11	Carbonate cement
FL38	(37.3433 °N, 117.8383 °W)	6.16	–	–	16.23	0.12	−4.71	0.09	Carbonate cement
FL39	(37.3433 °N, 117.8383 °W)	6.16	–	–	15.87	0.14	−2.88	0.11	Carbonate cement
FL40	(37.3433 °N, 117.8383 °W)	6.17	–	–	15.84	0.08	−4.54	0.08	Carbonate cement
FL41	(37.3433 °N, 117.8383 °W)	6.17	–	–	15.98	0.08	−4.24	0.06	Carbonate cement
FL42	(37.3433 °N, 117.8383 °W)	6.18	–	–	16.14	0.10	−3.75	0.12	Carbonate cement
FL43	(37.3433 °N, 117.8383 °W)	6.19	–	–	15.63	0.07	−4.89	0.05	Carbonate cement
FL44	(37.3433 °N, 117.8383 °W)	6.20	–	–	15.35	0.08	−5.12	0.06	Carbonate cement
FL47	(37.3433 °N, 117.8383 °W)	6.24	–	–	15.21	0.12	0.27	0.11	Caliche on basalt
FL49	(37.3433 °N, 117.8383 °W)	6.26	–	–	15.85	0.09	−2.67	0.07	Carbonate cement
FL52	(37.3433 °N, 117.8383 °W)	6.28	–	–	15.62	0.04	−4.19	0.07	Carbonate cement
FL53	(37.3433 °N, 117.8383 °W)	6.28	–	–	16.16	0.06	−2.67	0.05	Carbonate cement
FL55	(37.3433 °N, 117.8383 °W)	6.30	–	–	16.56	0.08	−2.50	0.07	Carbonate cement
Black Hole (Section S1)									
FL76	(37.3675 °N, 117.7887 °W)	4.10	–	–	15.86	0.11	−7.92	0.10	Caliche in green paleosol
FL75	(37.3675 °N, 117.7887 °W)	4.14	–	–	16.07	0.09	−8.05	0.08	Caliche in red paleosol
FL74	(37.3675 °N, 117.7887 °W)	4.16	–	–	15.70	0.08	−7.54	0.14	Carbonate root cast in paleosol
FL73	(37.3675 °N, 117.7887 °W)	4.18	–	–	16.36	0.10	−7.18	0.07	Carbonate cemented paleosol
FL72	(37.3675 °N, 117.7887 °W)	4.37	–	–	16.61	0.08	−7.60	0.10	Carbonate cemented paleosol
FL71	(37.3675 °N, 117.7887 °W)	4.45	–	–	15.61	0.08	−7.59	0.12	Carbonate cemented paleosol
FL70	(37.3675 °N, 117.7887 °W)	4.46	–	–	15.68	0.10	−7.94	0.06	Carbonate cemented paleosol
FL69	(37.3675 °N, 117.7887 °W)	4.56	–	–	15.41	0.08	−8.06	0.08	Carbonate in sandstone
FL68	(37.3675 °N, 117.7887 °W)	4.58	–	–	15.83	0.08	−7.72	0.08	Carbonate root cast in paleosol

(*continued on next page*)

Table 1 (*continued*)

Sample	Location	Age (Ma)	δD (‰ VSMOW)	δD Error (1σ)	δ^{18}O (‰ VSMOW)	δ^{18}O Error (1σ)	δ^{13}C (‰ VPDB)	δ^{13}C Error (1σ)	Material
FL67	(37.3675 °N, 117.7887 °W)	4.58	–	–	15.84	0.06	−7.35	0.03	Carbonate root cast in paleosol
FL66	(37.3675 °N, 117.7887 °W)	4.68	–	–	15.24	0.08	−7.08	0.16	Carbonate in sandstone
FL65	(37.3675 °N, 117.7887 °W)	4.64	–	–	16.09	0.07	−7.22	0.09	Carbonate cemented paleosol
FL64	(37.3675 °N, 117.7887 °W)	4.66	–	–	15.41	0.11	−7.28	0.11	Carbonate cemented paleosol
FL63	(37.3675 °N, 117.7887 °W)	4.67	–	–	15.49	0.06	−6.98	0.12	Carbonate cemented paleosol
FL61	(37.3675 °N, 117.7887 °W)	4.78	–	–	15.54	0.05	−6.57	0.15	Carbonate in tephra
FL60	(37.3675 °N, 117.7887 °W)	4.80	–	–	17.00	0.10	−6.52	0.10	Carbonate in sandstone
FL59	(37.3675 °N, 117.7887 °W)	4.92	–	–	15.17	0.13	−7.55	0.09	Carbonate in mudstone
FL58	(37.3675 °N, 117.7887 °W)	5.11	–	–	15.37	0.06	−7.11	0.06	Carbonate in conglomerate
Playa (Section S4)									
FL113	(37.3717 °N, 117.7925 °W)	2.29	–	–	27.04	0.07	1.45	0.06	Carbonate cement
FL109	(37.3717 °N, 117.7925 °W)	2.47	–	–	19.91	0.05	−1.62	0.07	Carbonate cement
FL104	(37.3717 °N, 117.7925 °W)	2.59	–	–	23.55	0.06	2.20	0.06	Carbonate cement
FL100	(37.3717 °N, 117.7925 °W)	2.83	–	–	25.38	0.09	−0.41	0.07	Carbonate cement
Badlands (Section S6)									
FL133	(37.3817 °N, 117.7900 °W)	1.48	–	–	17.67	0.07	−7.05	0.09	Carbonate cement
FL131	(37.3817 °N, 117.7900 °W)	2.08	–	–	16.51	0.03	−6.94	0.03	Carbonate cement
FL130	(37.3817 °N, 117.7900 °W)	2.16	–	–	17.47	0.04	−7.05	0.06	Carbonate cement
FL129	(37.3817 °N, 117.7900 °W)	2.23	–	–	17.42	0.06	−7.05	0.02	Carbonate cement
FL128	(37.3817 °N, 117.7900 °W)	2.31	–	–	17.05	0.07	−6.76	0.04	Carbonate cement
FL127	(37.3817 °N, 117.7900 °W)	2.46	–	–	17.52	0.05	−7.01	0.04	Carbonate cement
FL125	(37.3817 °N, 117.7900 °W)	2.61	–	–	16.98	0.06	−7.13	0.06	Carbonate cement
FL124	(37.3817 °N, 117.7900 °W)	2.69	–	–	17.81	0.07	−6.80	0.06	Carbonate cement
FL119	(37.3817 °N, 117.7900 °W)	3.10	–	–	17.60	0.10	−7.31	0.10	Carbonate cement

in FLV or VB. Nonetheless, several drivers are commonly associated with increases in δ^{18}O or δD: 1) Increases in δD or δ^{18}O, particularly in lacustrine carbonates, can be accommodated by increases in evaporative kinetic fractionation, 2) Increased evapotranspiration, and therefore moisture recycling, can lead to increased δ^{18}O values (e.g., Mix et al., 2013; Chamberlain et al., 2014; Winnick et al., 2014), and 3) Changes in seasonality of precipitation or moisture source can systematically affect the isotopic composition of precipitation. In the case of evaporation, there is evidence that late Cenozoic North America became progressively cooler and more arid (Eronen et al., 2012). However, this was a regional trend that would have driven synchronous changes at all three sites and not just in CB. With respect to evapotranspiration, the greatest effects would be expected at inland sites as moisture recycling reduces the Rayleigh distillation of atmospheric moisture. In contrast to the expected shallowing of the coast-interior stable isotope gradient, the most inland site (FLV) exhibits no increase in δ^{18}O while CB does, eliminating changes in evapotranspiration as a major driver in the late Cenozoic eastern Sierra and western Basin and Range. Finally, changes in the seasonality of precipitation and/or air mass trajectories (independent of those associated with coevolution of topography) are unlikely to produce the changes observed in these late Cenozoic records. Modern back-trajectories are similar in most seasons except for the summer months, where the influence of the North American Monsoon and water vapor recycling in the Basin and Range are apparent (**Supp. Fig. 1**). While southerly trajectories from the Gulf of California during the monsoon can deliver high-δ^{18}O moisture, the southern Owens Valley receives nearly all of its total precipitation during the winter and spring months, where Pacific-sourced moisture typically follows the wrap-around path (Intellicast, 2018) (Fig. 3). Thus, we interpret the stable isotope records from VB, CB and FLV to be robust archives of changes in circulation specific to the Sierra Nevada.

5. Conclusion

Three late Cenozoic stable isotope records provide insight into the history of atmospheric flow deflection around the southern (High) Sierra. These leeward records are relatively consistent throughout the late Cenozoic, suggesting that terrain blocking is a long-standing feature. These new observations are broadly consistent with atmospheric modeling studies suggesting that the Sierra Nevada had ideal geometric characteristics for producing terrain blocking effects (Galewsky, 2009a, 2009b). Given that these records remain unchanged during the late Cenozoic, our findings are consistent with the modeling work of Wheeler et al. (2016), suggesting that a warmer and more stable atmosphere allowed for terrain blocking effects as low as 2 km. A 1-2‰ increase in CB δ^{18}O values may suggest a slight increase in terrain blocking consistent with modest late Cenozoic uplift and/or the findings of Lechler and Galewsky (2013).

The Sierra Nevada continues to represent an ideal range to test and refine paleoaltimetry approaches. Pioneering work in the Basin and Range demonstrated the role of high topography in driving Rayleigh distillation and the northern Sierra became an ideal case study for a wave of windward paleoaltimetry studies. A lack of windward Cenozoic sediments and complications in interpreting distal leeward records in the southern Sierra, however, have presented a challenge for researchers. Accurate and well-constrained paleoclimate and paleoaltimetry reconstructions in the future will require both refinements in modeling techniques and the targeted development of stable isotope records to examine the complex and linked evolution of topography and atmospheric circulation.

Acknowledgements

This research was supported by National Science Foundation grants EAR-0309011 and EAR-1019648, and a Santa Clara University Sustainability Research Initiative grant to Mix. Caves was supported by an NSF Graduate Research Fellowship, a Stanford Graduate Fellowship, and an ETH Fellowship. This work was greatly improved by the constructive comments of Alex Lechler, Manny Gabet and Joe Galewsky. We thank Daniel Ibarra for helpful conversation, Peter Blisniuk and Walter Torres for lab and field assistance, and Michelle Bezanson for illustration of Fig. 3.

Appendix A. Supplementary material

Supplementary material related to this article can be found online at https://doi.org/10.1016/j.epsl.2019.04.050.

References

Badgley, C., Smiley, T.M., Finarelli, J.A., 2014. Great Basin mammal diversity in relation to landscape history. J. Mammal. 95, 1090–1106.

Bershaw, J., Penny, S.M., Garzione, C.N., 2012. Stable isotopes of modern water across the Himalaya and eastern Tibetan plateau: implications for estimates of paleoelevation and paleoclimate. J. Geophys. Res., Atmos. 117, D02110.

Blisniuk, P.M., Stern, L.A., 2005. Stable isotope paleoaltimetry: a critical review. Am. J. Sci. 305, 1033–1074.

Cassel, E.J., Graham, S.A., Chamberlain, C.P., 2009. Cenozoic tectonic and topographic evolution of the northern Sierra Nevada, California, through stable isotope paleoaltimetry in volcanic glass. Geology 37, 547–550.

Caves, J.K., Sjostrom, D.J., Mix, H.T., Winnick, M.J., Chamberlain, C.P., 2014. Aridification of Central Asia and uplift of the Altai and Hangay mountains, Mongolia: stable isotope evidence. Am. J. Sci. 314, 1171–1201.

Caves, J.K., Bayshashov, B.U., Zhamangara, A., Ritch, A.J., Ibarra, D.E., Sjostrom, D.J., Mix, H.T., Winnick, M.J., Chamberlain, C.P., 2017. Late miocene uplift of the Tian Shan and Altai and reorganization of Central Asia climate. GSA Today 27.

Chamberlain, C.P., Winnick, M.J., Mix, H.T., Chamberlain, S.D., Maher, K., 2014. The impact of neogene grassland expansion and aridification on the isotopic composition of continental precipitation. Glob. Biogeochem. Cycles. https://doi.org/10.1002/2014GB004822.

Clark, M.K., 2007. The significance of paleotopography. Rev. Mineral. Geochem. 66, 1–21.

Crowley, B.E., Koch, P.L., Davis, E.B., 2008. Stable isotope constraints on the elevation history of the Sierra Nevada mountains, California. GSA Bull. 120, 588–598.

Dansgaard, W., 1964. Stable isotopes in precipitation. Tellus 16, 436–468.

Draxler, R.R., Hess, G.D., 1998. An overview of the HYSPLIT_4 modelling system for trajectories. Aust. Meteorol. Mag. 47, 295–308.

Ducea, M.N., Saleeby, J.B., 1996. Buoyancy sources for a large, unrooted mountain range, the Sierra Nevada, California: evidence from xenolith thermobarometry. J. Geophys. Res., Solid Earth 101, 8229–8244.

Eronen, J.T., Fortelius, M., Micheels, A., Portmann, F.T., Puolamäki, K., Janis, C.M., 2012. Neogene aridification of the Northern Hemisphere. Geology 40, 823–826.

Friedman, I., Harris, J.M., Smith, G.L., Johnson, C.A., 2002. Stable isotope composition of waters in the Great Basin, United States 1. Air-mass trajectories. J. Geophys. Res. 107 (DX). ACL 14-1–14-13.

Gabet, E.J., 2014. Late Cenozoic uplift of the Sierra Nevada, California? A critical analysis of the geomorphic evidence. Am. J. Sci. 314, 1224–1257.

Galewsky, J., 2009a. Rain shadow development during the growth of mountain ranges: an atmospheric dynamics perspective. J. Geophys. Res., Earth Surf. 114, F01018.

Galewsky, J., 2009b. Orographic precipitation isotopic ratios in stratified atmospheric flows: implications for paleo-elevation studies. Geology 37, 791–794.

Horton, T.W., Chamberlain, C.P., 2006. Stable isotopic evidence for Neogene surface downdrop in the central Basin and Range province. GSA Bull. 118, 475–490.

Hren, M.T., Pagani, M., Erwin, D.M., Brandon, M., 2010. Biomarker reconstruction of the early Eocene paleotopography and paleoclimate of the northern Sierra Nevada. Geology 38, 7–10.

Intellicast, 2018. Historic average, Lone Pine, CA. http://www.intellicast.com/Local/History.aspx?location=USCA0630. (Accessed 15 November 2018).

Lechler, A.R., Galewsky, J., 2013. Refining paleoaltimetry reconstructions of the Sierra Nevada, California, using air parcel trajectories. Geology 41, 259–262.

Martel, S.J., Stock, G.M., Ito, G., 2014. Mechanics of relative and absolute displacements across normal faults, and implications for uplift and subsidence along the eastern escarpment of the Sierra Nevada, California. Geosphere 10, 243.

Mix, H.T., Winnick, M.J., Mulch, A., Chamberlain, C.P., 2013. Grassland expansion as an instrument of hydrologic change in Neogene western North America. Earth Planet. Sci. Lett. 377–378, 73–83.

Mix, H.T., Chamberlain, C.P., 2014. Stable isotope records of hydrologic change and paleotemperature from smectite in Cenozoic western North America. Geochim. Cosmochim. Acta 141, 532–546.

Mix, H.T., Ibarra, D.E., Mulch, A., Graham, S.A., Chamberlain, C.P., 2015. A hot and high Eocene Sierra Nevada. GSA Bull. 128, 531–542.

Molnar, P., 2010. Deuterium and oxygen isotopes, paleoelevations of the Sierra Nevada, and Cenozoic climate. GSA Bull. 122, 1106–1115.

Moore, D.M., Reynolds Jr., R.C., 1997. X-Ray Diffraction and the Identification and Analysis of Clay Minerals, second ed. Oxford University Press, New York.

Mulch, A., Graham, S.A., Chamberlain, C.P., 2006. Hydrogen isotopes in Eocene river gravels and paleoelevation of the Sierra Nevada. Science 313, 87–89.

Mulch, A., Sarna-Wojcicki, A.M., Perkins, M.E., Chamberlain, C.P., 2008. A Miocene to Pleistocene climate and elevation record of the Sierra Nevada (California). Proc. Natl. Acad. Sci. USA 105, 6819–6824.

Mulch, A., 2016. Stable isotope paleoaltimetry and the evolution of landscapes and life. Earth Planet. Sci. Lett. 433, 180–191.

Poage, M.A., Chamberlain, C.P., 2001. Empirical relationships between elevation and the stable isotope composition of precipitation and surface waters: considerations for studies of paleoelevation change. Am. J. Sci. 301, 1–15.

Poage, M.A., Chamberlain, C.P., 2002. Stable isotopic evidence for a Pre-Middle Miocene rain shadow in the western Basin and Range: implications for the paleotopography of the Sierra Nevada. Tectonics 21. https://doi.org/10.1029/2001TC001303.

Poppe, L.J., Paskevich, V.F., Hathaway, J.C., Blackwood, D.S., 2001. A Laboratory Manual for X-ray Powder Diffraction. USGS Open File Report 01-041.

Poulsen, C.J., Jeffery, M.L., 2011. Climate change imprinting on stable isotopic compositions of high-elevation meteoric water cloaks past surface elevations of major orogens. Geology 39, 595–598.

Reheis, M.C., Sarna-Wojcicki, A.M., Burbank, D.M., Meyer, C.E., 1991. The late Cenozoic section at Willow Wash, west-central California—a tephrochronologic Rosetta Stone. In: Reheis, M.C., Slate, J.L., Sawyer, T.L., Sarna-Wojcicki, A.M., Harden, J.W., Pendall, E.G., Gillespie, A.R., Burbank, D.M. (Eds.), Guidebook for Field Trip to Fish Lake Valley, California-Nevada. Friends of the Pleistocene, Pacific Cell, pp. 46–66.

Rohrmann, A., Strecker, M.R., Bookhagen, B., Mulch, A., Sachse, D., Pingel, H., Alonso, R.N., Schildgen, T.F., Montero, C., 2014. Can stable isotopes ride out the storms? The role of convection for water isotopes in models, records, and paleoaltimetry studies in the central Andes. Earth Planet. Sci. Lett. 407, 187–195.

Rowley, D.B., Pierrehumbert, R.T., Currie, B.S., 2001. A new approach to stable isotope-based paleoaltimetry: implications for paleoaltimetry and paleohypsometry of the High Himalaya since the Late Miocene. Earth Planet. Sci. Lett. 188, 253–268.

Rutz, J.J., Steenburgh, W.J., Ralph, F.M., 2015. The inland penetration of atmospheric rivers over Western North America: a Lagrangian analysis. Mon. Weather Rev. 143, 1924–1944.

Seager, R., Battisti, D., Gordon, J.Y.N., Naik, N., Clement, A., Cane, M., 2002. Is the Gulf Stream responsible for Europe's mild winters? Q. J. R. Meteorol. Soc. 128, 2563–2586.

Sjostrom, D.J., Welker, J.M., 2009. The influence of air mass source on the seasonal isotopic composition of precipitation, eastern USA. J. Geochem. Explor. 102, 103–112.

Stock, G.M., Anderson, R.S., Finkel, R.C., 2004. Pace of landscape evolution in the Sierra Nevada, California, revealed by cosmogenic dating of cave sediments. Geology 32, 193–196.

Taylor, H.P., 1974. The application of oxygen and hydrogen isotope studies to problems of hydrothermal alteration and ore deposition. Econ. Geol. 69, 843–883.

Trexler, J., Cashman, P., Cosca, M., 2012. Constraints on the history and topography of the northeastern Sierra Nevada from a Neogene sedimentary basin in the Reno-Verdi area, Western Nevada. Geosphere 8, 548–561.

Wang, Y., Forsyth, D.W., Rau, C.J., Carriero, N., Schmandt, B., Gaherty, J.B., Savage, B., 2013. Fossil slabs attached to unsubducted fragments of the Farallon plate. Proc. Natl. Acad. Sci. 110, 5342–5346.

Wheeler, L.B., Galewsky, J., Herold, N., Huber, M., 2016. Late Cenozoic surface uplift of the southern Sierra Nevada (California, USA): a paleoclimate perspective on lee-side stable isotope paleoaltimetry. Geology 44, 451–454.

Winnick, M.J., Chamberlain, C.P., Caves, J.K., Welker, J.M., 2014. Quantifying the isotopic "continental effect". Earth Planet. Sci. Lett. 406, 123–133.

Zandt, G., Gilbert, H., Owens, T.J., Ducea, M., Saleeby, J., Jones, C.H., 2004. Active foundering of a continental arc root beneath the southern Sierra Nevada in California. Nature 431, 41–46.